Defect Structures in the Growth Kinetics of the Swift-Hohenberg Model

Hai Qian and Gene F. Mazenko

James Franck Institute and Department of Physics, University of Chicago, Chicago, Illinois 60637

(Oct. 18, 2002)

The growth of striped order resulting from a quench of the two-dimensional Swift-Hohenberg model is studied in the regime of a small control parameter and quenches to zero temperature. We introduce an algorithm for finding and identifying the disordering defects (dislocations, disclinations and grain boundaries) at a given time. We can track their trajectories separately. We find that the coarsening of the defects and lowering of the effective free energy in the system are governed by a growth law $L(t) \approx t^x$ with an exponent x near 1/3. We obtain scaling for the correlations of the nematic order parameter with the same growth law. The scaling for the order parameter structure factor is governed, as found by others, by a growth law with an exponent smaller than x and near to 1/4. By comparing two systems with different sizes, we clarify the finite size effect. We find that the system has a very low density of disclinations compared to that for dislocations and fraction of points in grain boundaries. We also measure the speed distributions of the defects at different times and find that they all have power-law tails and the average speed decreases as a power law.

I. INTRODUCTION

What are the defects which control the long-time ordering of systems growing a striped pattern? This question arises in a variety of physical contexts [1]. Here we are motivated by the recent experiments [2,3] investigating the ordering of a two dimensional diblock copolymer system. The system studied offers a physical realization of the ordering in an isotropic two-dimensional smectic material. In these experiments they found that the late-time ordering satisfies scaling with a growth law $L \approx t^x$ with $x = 1/4$ and the final stages of ordering are governed by the annihilation of sets of disclination quadrapoles. In this paper we address the question: Is the ordering in this physical system described by the Swift-Hohenberg (SH) model [4], the simplest model one can construct to govern the ordering in stripe forming systems?

We investigate the growth kinetics of the Swift-Hohenberg model for a small control parameter ($\epsilon = 0.1$) in two dimensions and quenches to zero temperature. It is this regime which appears most likely to correspond to the experimental situation. In large ϵ regime the system evolves to a glassy state. We focus primarily on the defect structures generated in the ordering of the system. In the most naive picture of this ordering process one can think in terms of an initial local layering, as in a smectic, in some direction. This ordering can be disrupted by point defects: dislocations and disclinations. This suggests a coarsening picture with annihilating point defects similar to the case of the XY model [5] and a growth law with exponent $x = 1/2$. This simple picture is not seen in simulations. We find, in agreement with the numerical results of Hou *et al.* [6] and Boyer and Viñals [7], that the defect structures for the SH model are dominated by grain boundaries which persist for long times. Unlike the case of an XY model, the ordering is not dominated by

annihilation of isolated point defects. These are observed but are not the dominant structures.

We find numerically, at late times after finite size effects enter, that the system becomes anisotropic, and the grain boundaries shrink. In this case one sees a cross-over to an effective growth exponent $x = 1/2$.

We give below a detailed numerical study of the statistical properties of the defects disrupting striped pattern formation in the SH model. In order to carefully discuss the defects we need a reliable filter for finding them. We present an algorithm which effectively locates defects and grain boundaries for any control parameter ϵ. We can distinguish between grain boundaries and other defects, and track their trajectories separately. We compare this method to the other approaches used in earlier work in appendix A.

There are a number of ways of characterizing the degree of ordering in these systems: (i) Counting the number and size of defects and their evolution with time. (ii) Monitoring the lowering of the average effective driving free energy as a function of time. (iii) Evaluation of the nematic order parameter correlation function and its associated scaling behavior. (iv) Evaluation of the order parameter structure factor and its associated scaling behavior. We find that (i), (ii), and (iii) can all be characterized by a single growth law with the exponent near 1/3, while the order parameter scaling, as found by others, is characterized by a growth law with the exponent near 1/5.

II. SWIFT-HOHENBERG MODEL

The Swift-Hohenberg model for a scalar order parameter, ψ, is specified by the equation of motion

$$\frac{\partial \psi}{\partial t} = \epsilon \psi - \psi^3 - \left(q_0^2 + \nabla^2\right)^2 \psi + \zeta , \qquad (1)$$

where ϵ is a positive control parameter, q_0 is the magnitude of an ordering wavenumber and ζ is the Gaussian noise satisfying $\langle \zeta(\mathbf{r},t)\zeta(\mathbf{r}',t') \rangle = 2\Gamma\delta(\mathbf{r} - \mathbf{r}')\delta(t - t')$, where the noise strength Γ is proportional to the final temperature governing the system after a quench. We will focus here on quenches to zero temperature where we can set Γ and the noise ζ to zero. We are interested in the growth kinetics problem where we prepare this system initially in a completely disordered state. We then allow the system to evolve forward in time to form a striped pattern. For example one could choose

$$\langle \psi(\mathbf{x}, t_0)\psi(\mathbf{y}, t_0) \rangle = \Psi_0^2 \, \delta\left(\mathbf{x} - \mathbf{y}\right) , \qquad (2)$$

where Ψ_0^2 is a constant. However the precise form of the initial conditions is not important [5].

This model can be formulated as a Langevin equation driven by an effective Hamiltonian:

$$\mathcal{H}_E = \int d^2x \left\{ -\frac{\epsilon}{2}\psi^2 + \frac{1}{4}\psi^4 + \frac{1}{2}\left[\left(q_0^2 + \nabla^2\right)\psi\right]^2 \right\} . \quad (3)$$

If we introduce

$$E(t) = \langle \mathcal{H}_E \rangle_t , \qquad (4)$$

where the average is over an ensemble of initial conditions, then $E(t)$ is lowered as the system orders in a striped pattern with wavenumber q_0.

Eventually the system approaches an ordered state described approximately by the single-mode approximation [8] where, assuming layering along the z-direction,

$$\psi_0 = A_0 \, \cos q_0 z . \qquad (5)$$

If we put this ansatz into Eq.(3), assume that the system is an integral number of wavelengths in the z-direction, and minimize with respect to the amplitude A_0, we obtain the results,

$$A_0^2 = \frac{4\epsilon}{3} , \qquad (6)$$

$$\langle \psi_0^2 \rangle = \frac{q_0}{2\pi} \int_0^{2\pi/q_0} (A_0 \, \cos q_0 z)^2 \, dz = \frac{2\epsilon}{3} , \qquad (7)$$

and

$$E_{eq} = -\frac{\epsilon^2}{6}S , \qquad (8)$$

where S is the area of the system. Pomeau and Manneville [8] have shown that this is a very good approximation for the "ground" state even for moderately large values of ϵ. In the growth kinetics context the approach to equilibrium is monitored by

$$\Delta E(t) \equiv E(t) - E_{eq} \propto L_E^{-1}(t) , \qquad (9)$$

and

$$\Delta \psi^2(t) \equiv \langle \psi_0^2 \rangle - \langle \psi^2 \rangle_t \propto L_\psi^{-1}(t) , \qquad (10)$$

where $L_E(t) \propto L_\psi(t)$ [9].

Another measure of the ordering in the system is given by considering the director field

$$\hat{n}(\mathbf{x}) = \frac{\nabla \psi(\mathbf{x})}{|\nabla \psi(\mathbf{x})|} , \qquad (11)$$

and the associated nematic order parameter

$$Q_{\alpha\beta} = Q_0 \left[\hat{n}_\alpha \hat{n}_\beta - \frac{1}{2}\delta_{\alpha\beta} \right] . \qquad (12)$$

In two dimensions, however, all of the information in this order parameter is contained in the quantity $\cos 2\theta$ where $\hat{n} = (\cos\theta, \sin\theta)$. It is easy to show, for example, that

$$C_{nn}(\mathbf{x}, \mathbf{y}, t) \equiv 2\langle \operatorname{Tr} \mathrm{Q}(\mathbf{x}, \mathrm{t})\mathrm{Q}(\mathbf{y}, \mathrm{t}) \rangle_{\mathrm{t}}$$
$$= \langle \cos\left[(\varphi(\mathbf{x}, t) - \varphi(\mathbf{y}, t)\right] \rangle_t . \qquad (13)$$

where

$$\varphi(\mathbf{x}, t) = 2\theta(\mathbf{x}, t) . \qquad (14)$$

If we define

$$\hat{B}_x = \hat{n}_x^2 - \hat{n}_y^2 \qquad (15)$$

$$\hat{B}_y = 2\hat{n}_x \hat{n}_y \qquad (16)$$

then

$$C_{nn}(\mathbf{x}, \mathbf{y}, t) = \langle \hat{B}(\mathbf{x}, t) \cdot \hat{B}(\mathbf{y}, t) \rangle_t . \qquad (17)$$

The nematic order parameter correlation function, C_{nn}, was shown by Christensen and Bray [10] to obey scaling in the conventional form

$$C_{nn}(\mathbf{r}, t) = F\left(r/L_n(t)\right) , \qquad (18)$$

where $\mathbf{r} = \mathbf{x} - \mathbf{y}$. Elder, Viñals and Grant [11] showed that the scaling of the order parameter structure factor

$$S(k, t) = \langle |\psi_{\mathbf{k}}(t)|^2 \rangle = L_s(t)F_1((k - q_0)L_s(t)) , \qquad (19)$$

differs from that observed in ordering system without stripes: $S(k, t) = L^2(t)F_2(kL(t))$.

III. REVIEW OF PREVIOUS WORK

The early work on this problem focused on establishing the final equilibrium state reached after a quench. This is a two dimensional system and by forming stripes one has a broken continuous symmetry. The behavior of the system at non-zero temperatures, as for the two dimensional X-Y model, requires, as pointed out by Toner and Nelson [12] a treatment of both long wavelength fluctuations in the layers and free defects. Above a Kosterlitz-Thouless type transition one has an isotropic phase while below this transition one has a phase with persistent orientational order.

In an early paper, Elder, Viñals, and Grant [11] carried out a numerical analysis leading to the scaling solution given by Eq.(19). Working with fixed $\epsilon = 0.25$ they looked at the system's ordering as a function of noise strength Γ. They found a qualitative difference between low noise and high noise. For the large noise case they found a rapid (exponential) relaxation to the asymptotic stationary state and a power-law approach for the lower noise case. Their results are in agreement with the picture due to Toner and Nelson that one has a transition to an isotropic state for large enough noise. There is no real ordering in the isotropic state and this is why there is exponential decay to the equilibrium state. In the ordered state one has scaling and a power-law growth law which, for small noise, they found to have an exponent $x_s = 1/4$. They found a smaller exponent $x_s = 1/5$ at low temperatures, but they had less statistics and there appeared to be "difficulty removing defects". They argued for a late time cross over to the *expected* $x = 1/2$ but they did not see this.

Cross and Meiron [13] also studied the SH model numerically in the absence of noise. They found a $x_s = 1/4$ for $\epsilon = 0.25$. The dynamics appear to freeze for higher ϵ. They looked at the defect structure but in a qualitative way noting the existence of domain walls rather than a set of isolated point defects. The theoretical discussion in their paper is based on the phase-field approximation

$$\frac{\partial \phi}{\partial t} = \left(D_\parallel \nabla_\parallel^2 + D_\perp \nabla_\perp^2 \right) \phi , \qquad (20)$$

which from the most naive point of view suggests a growth law with exponent $x = 1/2$. They discuss some selection mechanisms which could lead $D_\parallel$ and $D_\perp$ to adjust themselves to zero and reduce x to $1/3$ or $1/4$. They concluded that they did "not have a good theoretical understanding of these results" and suggested that the defects in the problems should be treated explicitly.

Hou, Sasa, and Goldenfeld (HSG) [6] confirmed previous numerical results which showed for $\epsilon = 0.25$, $x_s = 1/5$ with zero noise and $x_s = 1/4$ with nonzero noise as obtained from the structure factor scaling. They went further and used a simple method to identify domain walls and measure their lengths (more about this below). They measured excess energy, $\Delta E(t)$, and the domain wall length and found that they show the same scaling exponents $1/4$ at zero noise and 0.3 at non-zero noise. The energy does go to the lowest order in ϵ value of $-\epsilon^2/6$ in the noiseless limit. They find "defects are indeed the driving force behind the coarsening process due to its dominant contribution to the excess energy." They suggest that the phase field approach gives the wrong exponent because it does not include the effects of defects. For larger ϵ (=0.75) they found much slower logarithmic growth. The system seems to become glassy.

Christensen and Bray [10] also carried out numerical work on the SH model for $\epsilon = 0.25$ and found $x_s = 1/5$ for zero noise and $x_s = 1/4$ for nonzero noise. From scaling of the *director* correlation function they find exponents are 0.25 and 0.30 for zero and nonzero noise. They suggest that there is a cross over to $x = 1/2$ at very long times. The theory they developed does not include defects.

Boyer and Viñals [7] point out "Near the bifurcation threshold, the evolution of disordered configurations is dominated by grain boundary motion through a background of largely immobile curved stripes". They find for small ϵ an exponent $x = 1/3$ which they interpret as arising from a law of grain boundary motion [14]. Elsewhere [15] they also point out for larger values of ϵ the dynamics cross over to a frozen state with quenches to zero temperature. This glassy behavior is associated with grain boundary pinning.

IV. NUMERICAL RESULTS FOR SH MODEL

We present here our numerical results for the SH equation. We follow the numerical prescriptions of Bray and Christensen [10]. We use the finite difference scheme on two dimensional lattice of sizes 256×256 and 512×512 with periodic boundary conditions. We set $\epsilon = 0.1$, $\Delta r = \pi/4$ and $\Delta t = 0.03$. We replace $\partial_t \psi(\mathbf{r}, t)$ by $\left(\psi_{ij}^{n+1} - \psi_{ij}^n \right)/\Delta t$, and $\nabla^2 \psi(\mathbf{r}, t)$ by

$$\nabla^2 \psi_{ij} = \frac{1}{(\Delta x)^2} \left[\frac{2}{3} \sum_{NN} + \frac{1}{6} \sum_{NNN} - \frac{10}{3} \right] \psi_{ij} \qquad (21)$$

where NN and NNN mean the nearest neighbors and next-nearest neighbors respectively. By choosing the proper scale of time, space and the order parameter, we can set $q_0 = 1$. The systems have eight grid points per wavelength. We used uniformly distributed random initial conditions.

For the smaller 256×256 systems we were able to follow the ordering process to very late stages. Some of the independent trials proceed to a final state where we have a set of well aligned layers.

In Fig. 1 we plot $\Delta E(t)$ and $\Delta \psi^2(t)$ for an ensemble of runs on a 256×256 lattice. We note that there are two regimes where L_E defined by Eq.(9) is described by different exponents. For $t_s < t < t_c$ ($t_s \approx 300$ and $t_c \approx 9000$) we find $x_E \approx 0.3$, while for $t > t_c$ we find $x_E \approx 0.5$. The cross over at $t \approx t_c$ appears to be due to the finite size effects, as we discuss below. For $t > t_c$ the system is effectively anisotropic and we find an effective exponent x_E near to $1/2$.
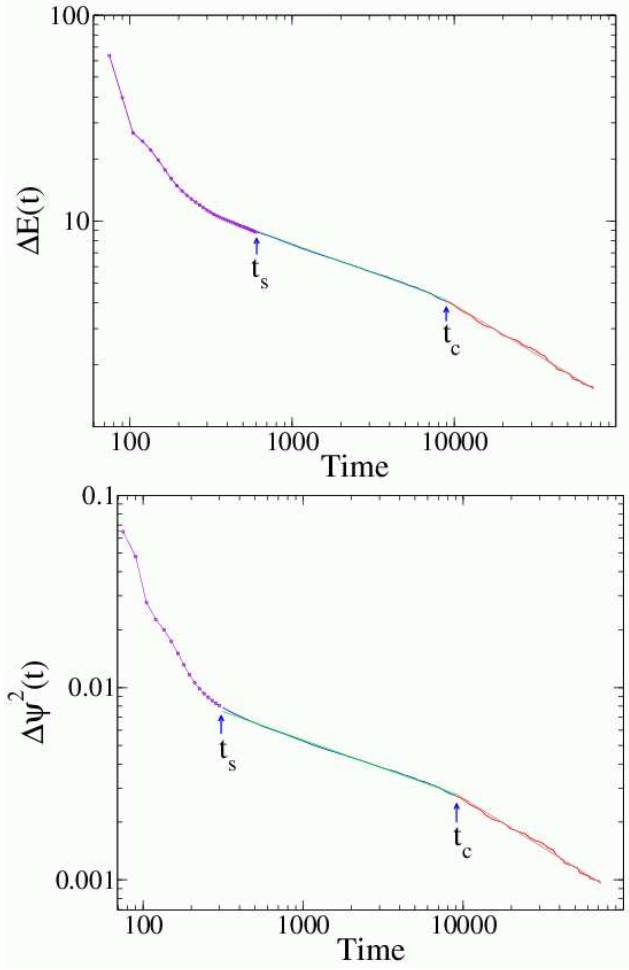
FIG. 1. $\Delta E(t)$ and $\Delta \psi^2(t)$ for a 256×256 system. Straight lines are used to fit different parts. Averaged over 40 trials.

In Fig. 2 we plot $\Delta E(t)$ and $\Delta \psi^2(t)$ for a 512×512 system. In this case we see that t_c has been extended to much larger values and we have not been able to follow the ordering process to completion. Our fits to $\Delta E(t)$ and $\Delta \psi^2(t)$ in the regime $t_s < t < t_c$ again gives, to higher accuracy, $x_E = x_\psi = 1/3$.
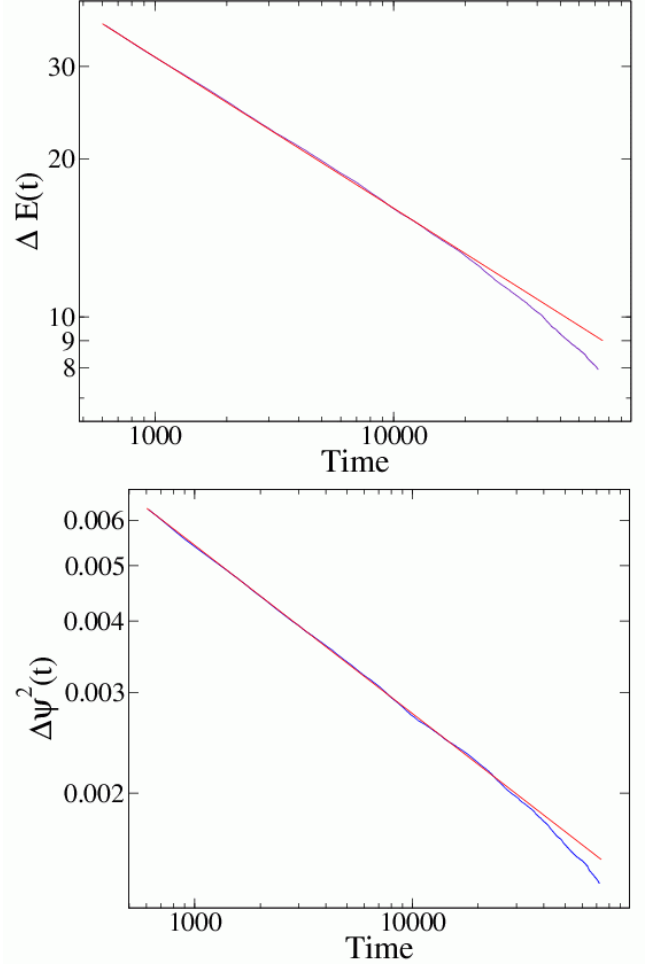

FIG. 2. $\Delta E(t)$ and $\Delta \psi^2(t)$ for a 512×512 system. The data for $t < t_s$ are not shown. The straight lines are used to guide eyes. Averaged over 57 different trials.

To probe directly the stripes' increasingly orientational order, we measure the *nematic* order parameter correlation function $C_{nn}(\mathbf{r}, \mathbf{t})$ in the 512×512 system. The results, averaged over 57 runs, are shown in Fig. 3. We obtain scaling with a correlation length obeying the growth law $L_n \propto t^{0.36}$. We can estimate the time t_c when the cross-over begins in this larger system as follows. The system becomes anisotropic and one expects cross-over when the correlation length L_n grows to be some substantial fraction of a lateral dimension of the system. In terms of ratios we can write

$$\frac{L_n(t_c(512))}{L_n(t_c(256))} \approx \frac{512}{256} = \left[\frac{t_c(512)}{t_c(256)}\right]^{1/3} \qquad . \qquad (22)$$

In the 256×256 system $t_c(256) \sim 9000$, so we obtain $t_c(512) \sim 60000$. Notice that in Fig. 2 the effective exponent x_E begins to increase at the time $50000 \sim 70000$, which is consistent with our estimate.
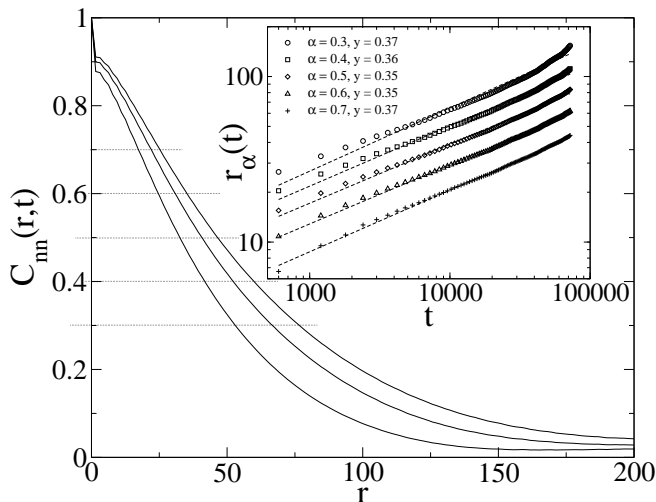
4

FIG. 3. Time evolution of the correlation function $C_{nn}(r,t)$ in 512×512 SH system illustrated with times $6\times10^3, 1.2\times10^4, 1.8\times10^4$ increasing from left to right. We extract the time evolution of the correlation length $L(t)$ by monitoring the $r_\alpha(t)$ for which $C_{nn}(r_\alpha(t)) = \alpha$, where we choose $\alpha = \{0.3, 0.4, 0.5, 0.6, 0.7\}$. The scaling exponent x_n is extracted from the log-log plot insert of $r_\alpha(t)$ v.s. t by fitting it with a straight line. Averaged over 57 trials.
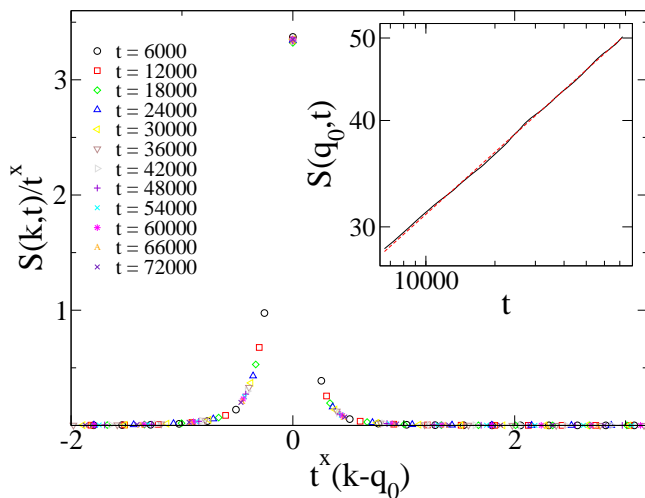
FIG. 4. The structure factor $S(k,t) = \langle|\psi(\mathbf{k},\mathbf{t})|^2\rangle$ in the 512×512 system. The log-log plot of $S(q_0,t)$ v.s. t can be fit to t^x with $x = 0.24$. The scaling collapse of the structure factor was obtained with $x = 0.24$ as the scaling exponent. Averaged over 57 independent trials.

In Fig. 4 we plot the structure factor $S(\mathbf{k},t)$ and show that scaling holds in the form given by Eq.(19) with a growth law characterized by an exponent $x_s = 0.24$ as shown in the insert. Our results here agree with those found previously that the exponent governing the growth law for the structure factor is significantly smaller than that governing the nematic order parameter.

V. DEFECT STRUCTURES AND DYNAMICS

In Fig. 5 we show a typical configuration for the Swift-Hohenberg model for a quench to zero temperature after a time 12000 for a 512×512 system. Notice the rather complicated structure which includes dislocations, disclinations and grain (domain) boundaries. Our main focus in this paper is to study the statistics of these defects. In appendix A we discuss an algorithm for picking out the defects and tracking their motions.
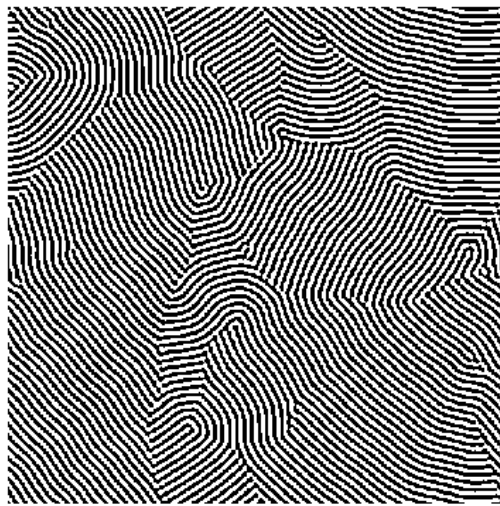

FIG. 5. A typical configuration for the SH model for a quench to zero temperature after $t = 12000$ in a 512×512 system. The black points correspond to $\psi(\mathbf{x}) > 0$, and the white points to $\psi(\mathbf{x}) < 0$.

If we look at Fig. 5 we see that it shows a complicated situation with a variety of different defect structures which one can identify by eye at the length scale of several layer spacings. At a more fundamental level we need a way of identifying which points in space, at the level of each site on the numerical grid, are part of a defect. At the shortest length scale in the problem the order parameter is $Q_{\alpha\beta}$ defined by Eq.(12). For this two-dimensional system this can be replaced by the vector order parameter $\hat{\mathbf{B}}$ defined by Eqs.(15) and (16). The assumption is that all of the defects in the system can be built up from the $\pm\frac{1}{2}$ disclinations in the director field $\hat{n}$ which translate into vortices with charge ±1 for the field $\hat{\mathbf{B}}$. We identify these defects by looking for the cores of the vortices. We can find the cores of the defects by looking from those sites where $\hat{\mathbf{B}}$ is changing rapidly. We can define

$$A = \sum_{\alpha,\beta} \left(\nabla_\alpha B_\beta\right)^2 \qquad (23)$$

and identify defect points as those sites where A is larger than some value. Notice that A can also be written in the form

$$A = 4 \sum_{\alpha,\beta} (\nabla_\alpha n_\beta)^2 = (\nabla_\alpha \varphi)^2 \quad . \tag{24}$$

The precise numerical determination of A is discussed in appendix A. Notice that A is proportional to the gradient energy for an isotropic nematic.

In analyzing their experimental data Harrison, et al. [2,3] found a set of *fundamental* disclinations and from these built up dislocations as bound disclinations with opposite charge. They used this procedure to identify a large dislocation density. Most of the fundamental disclinations went into forming these dislocations since in the end the ratio of dislocations to the remaining disclinations was about ten to one. In our case the situation is complicated by the grain boundaries. We first separate the defects into compact point defects and larger grain boundaries. For the point defects we determine the topological charge by taking the usual phase-angle path integral around the center of mass of the defect. Those defects with plus or minus unit charge are identified as disclinations, while those with zero charge are dislocations. Then we can track the motion of each single defect.
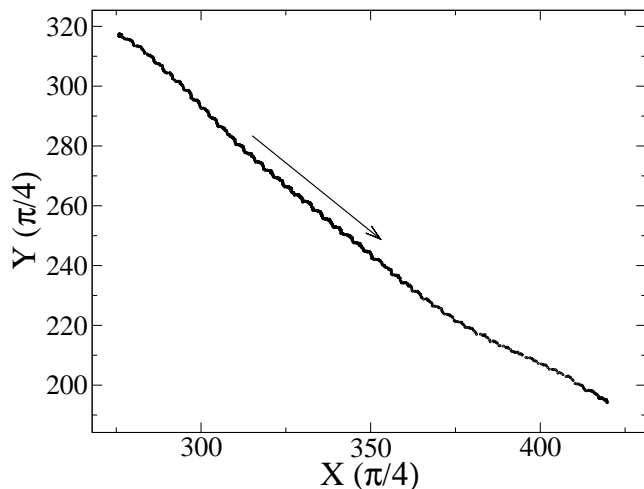
FIG. 6. A typical example of the track of a dislocation's "mass center", see appendix A. The dislocation moves along the arrow. It starts at $t = 1590$ and disappears at $t = 29220$. Notice the small arcs along the curve, the diameters of the arcs are about 2π, which is equal to two layer spacing.

As an example of the method we show in Fig. 6 the path of a dislocation. We see that some dislocations travel over long distances during very long times. It seems that the dislocations are more stable when compared to grain boundaries and disclinations. Our simulations on 256×256 system show that after the annihilation of point defects and grain boundaries, some dislocations still exist in the system. Our simulations show that there are also dislocations which are pinned and move little.

The number of disclinatins is quite small. And we notice that they are rather immobile, which is consistent with Boyer and Viñals' discussion [7].

The most important motion of grain boundaries is that they can move over long distances and combine with other grain boundaries. As shown in Fig. 7, two grain boundaries can combine to form a larger grain boundary. Thus the number of grain boundaries decreases while their average size increases. This process happens on a time scale of the order 1000 dimensionless time units.
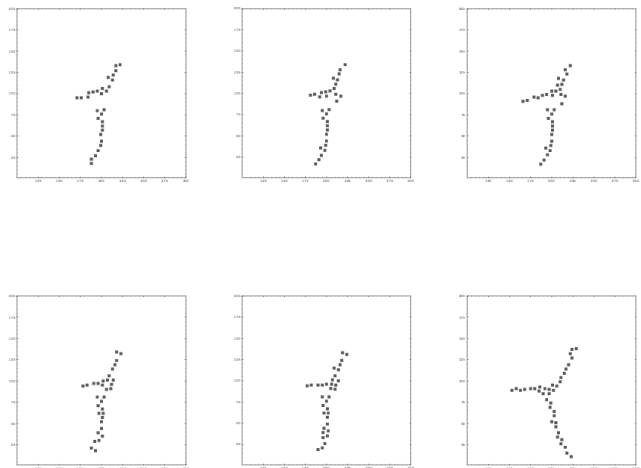
FIG. 7. The combination of two grain boundaries in a 512×512 system. The portion shown is 200×200. From left to right and top to bottom, the times are $t = 2880, 2955, 3030, 3105, 3180, 4710$. Not all the points in the grain boundaries are shown.
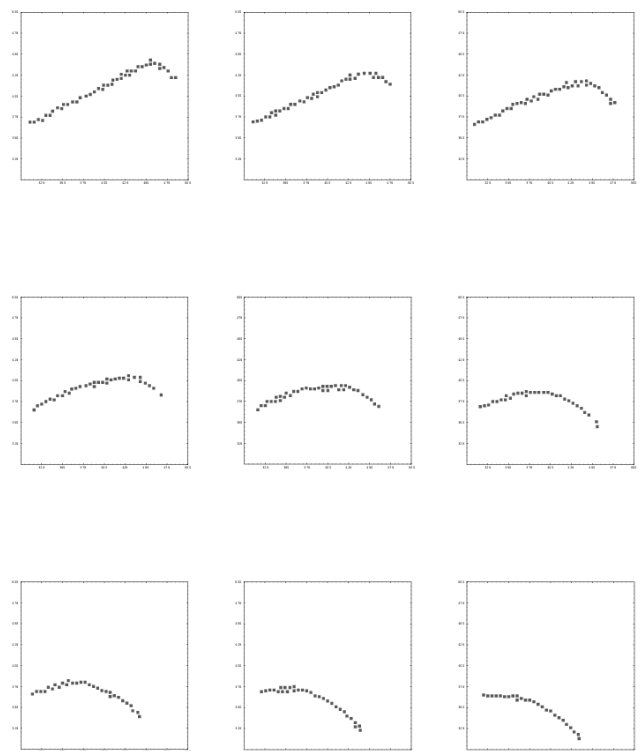
FIG. 8. The motion of a grain boundary in a 512×512 system. The portion shown is 200×200. From left to right and top to bottom, the times are $t = 11415, 13665, 15915, 18165, 20415, 22665, 24915, 27165, 29415$. Again not all the points in the grain boundary are shown.

As shown in Fig. 8, one grain boundary can sweep across a quite large area. At the same time its size decreases. This process occurs on a time scale of the order 10000. According to our observations, the grain boundaries' motions also relieve the stripe curvatures through disclination annihilations. After one grain boundary passes through a disclination, the disclination disappears. This is consistent with Boyer and Viñals' prediction [7].
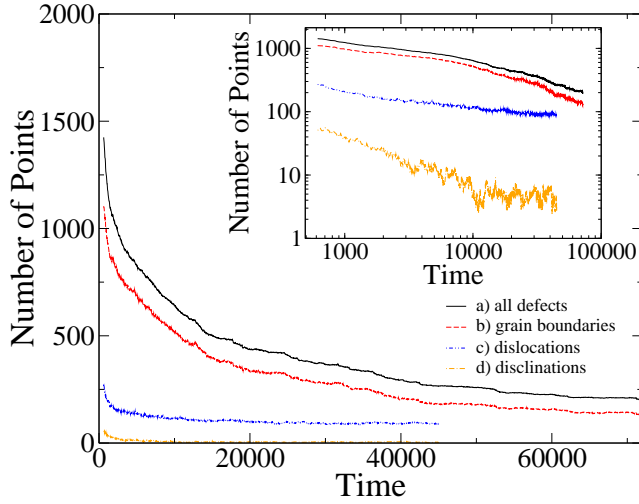

FIG. 10. The average number of grain boundaries and the average number of points in a grain boundary. 256×256 system averaged over 40 trials.

In Fig. 10 we plot the average number of grain boundaries $\bar{n}$ and the average size of a grain boundary $\bar{l}$ for the 256×256 system. We use the number of points in one grain boundary as a measure of its size. For $t_s < t < t_c$, $\bar{n}$ decreases but $\bar{l}$ increases due to the combining of grain boundaries. The shrinkage of their sizes is not as important as the combinations. However for $t_c \sim 9000$ the correlation length L_n is the same order as the system's size, and the large grain boundaries stop growing. After that the shrinkage is important [16]. In the scaling regime ($t_s < t < t_c$), $\bar{n} \sim t^{-0.45}$, and $\bar{l} \sim t^{0.13}$. So $\bar{n}\bar{l} \sim t^{-1/3}$, which is consistent with Fig. 9.

FIG. 9. The number of points in point defects and grain boundaries in the 256×256 system. The data for all defects and domain walls are averaged over 40 trials. The others are averaged over 38 trials.

Next we focus on the statistics of the defects generated by the model. In Fig. 9 we plot the total number of points in grain boundaries, dislocations and disclinations separately for the 256×256 system. We see that the grain boundaries dominate. In the scaling regime ($t_s < t < t_c$), we see that the number of points corresponding to grain boundaries and all defect points, the curves a and b can be fit to $\sim t^{-1/3}$. At late stages the disclinations disappear, while the dislocations and grain boundaries persist. The number of disclinations decreases much faster than the other defects.
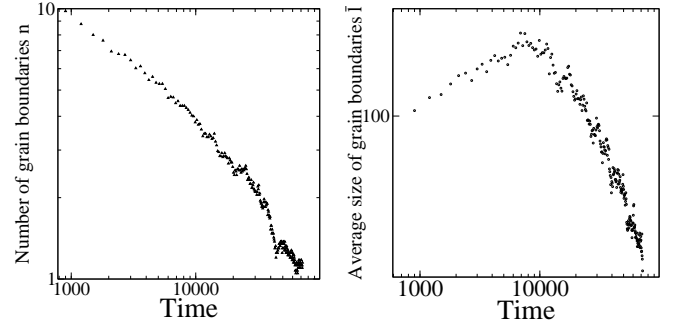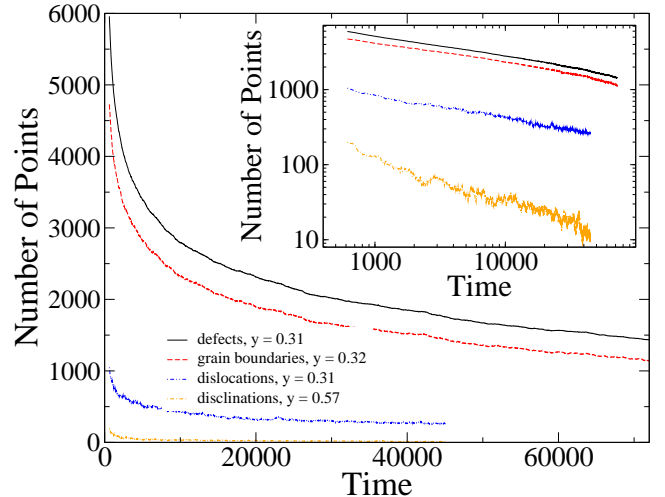

FIG. 11. The average number of points in defects and grain boundaries in the 512×512 system. Most of the points are in grain boundaries. All the curves can be fit to t^{-y}. The data for defects and domain walls are averaged over 57 trials, and the other data are averaged over 20 trials.
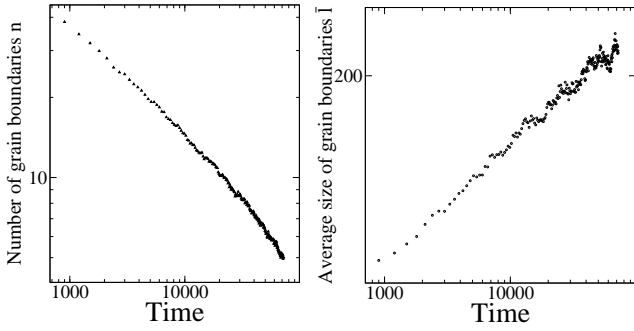
7

FIG. 12. $\bar{n}$ and $\bar{l}$ v.s. time in the 512×512 system. The data are averaged over 57 independent trials.

FIG. 13. A typical example of probability density P v.s. speed v for the speed distribution of dislocations at time 1350 for the 512×512 system. The distributions at other times have approximately the same shape. Averaged over 56 trials.

In Fig. 11 we plot the total number of points in grain boundaries, dislocations and disclinations separately for the 512×512 system. The number of points in disclinations is much smaller than that of dislocations and at very late stages it decreases to the order of 1, which in fact indicates the disappearance of disclinations. Now the scaling regime extends to much longer times. The domain walls and dislocations' scaling exponents are both $1/3$, which is same to the scaling of the energy. However, the scaling exponent of disclinations, given by 0.57 is much larger. So we conclude that disclinations are not the dominant structures in SH system.

In Fig. 12 we plot the number of grain boundaries $\bar{n}$ and the average size of a grain boundary $\bar{l}$ for 512×512 system. All of our data falls in the scaling regime.. The plot of the average number $\bar{n}$ of grain boundaries versus time t, can be fit to $\bar{n} \sim t^{-0.49}$ and the average size $\bar{l}$ v.s. time t, can be fit by $\bar{l} \sim t^{0.17}$. So we have $\bar{n}\bar{l} \sim L^{-1} \sim t^{-1/3}$, which is consistent with the results shown in Fig. 11.

Although we did not count the number of disclinations directly, it is proportional to the number of lattice points in disclinations, i.e. $t^{-0.57}$. This is because the average number of lattice points in one point disclination, which is about $10 \sim 20$, is quite stable during the simulation. By the same reasoning, we find that the number of dislocations is proportional to $t^{-1/3}$. It is interesting to note that the number of grain boundaries scales as $t^{-0.49}$. This exponent is near to that for disclinations.

The number of grain boundaries is about 5 at $t \sim 70000$, the number of disclinations is about 0 or 1 at $t \sim 50000$, and the number of dislocations is on the order of 10 at $t \sim 50000$, as can be seen in Figs. 11 and 12.
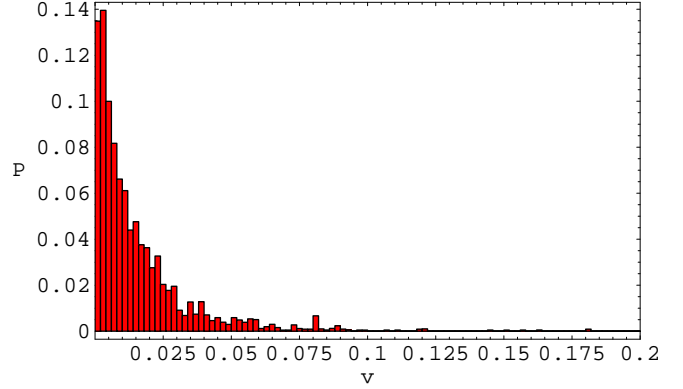
Since we can track the motion of each defect, we can measure their speeds. We define the speed of each as the speed of its mass center (see appendix A for the definition of "mass center"). If in a time $\Delta\tau$, the mass center travels over a distance Δd, then the speed is $v = \Delta d/\Delta\tau$. If $\Delta\tau$ is small enough, we found that $v = 0$ has the biggest probability.. If $\Delta\tau$ is large enough, all the details are coarse-grained and we observe a continuous distribution of the speed and the largest probability appears at a non-zero speed, as is shown in Fig. 13 where $\Delta\tau = 60$. We measured the speed distributions of domain walls and point defects separately. As we have already seen, for point defects the number of disclinations is much smaller than that of dislocations, so what we measure in the latter case is in fact the speed distribution of dislocations.

The speed distribution has a long tail which decreases as a power law. The numerical fits at different times give us different exponents. However the tail exponents at different times do distribute in a narrow region, as is shown in Fig. 14. The exponents of grain boundaries are quite different from those of point defects. If we ignore the exponents at very early times when grain boundaries just begin to form and at the very late times when the grain boundaries have already disappeared, the mean value of the grain boundaries' exponents is -1.50, and that of point defects' exponents is -2.10.
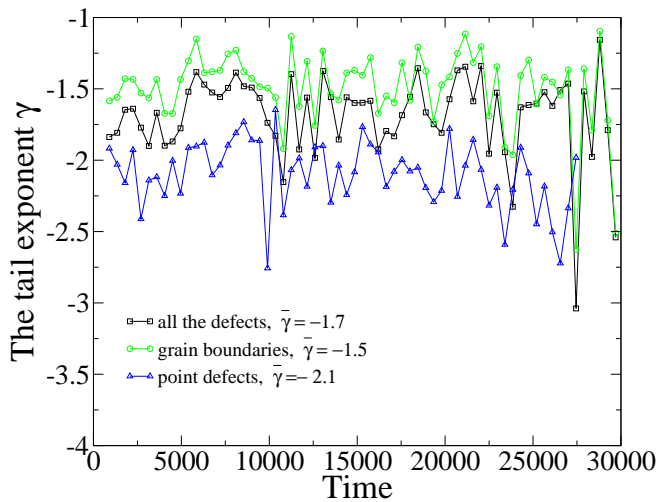
8

FIG. 14. The power law exponents of the speed distribution's tail at different times. Ignoring the data points at very early times and very late times, the mean value of the exponents is -1.5 for grain boundaries, -2.1 for point defects and -1.7 for all the defects. Averaged over 61 independent trials.
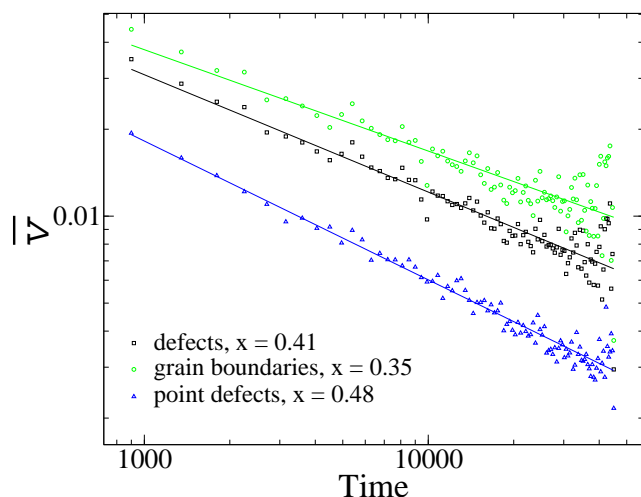

FIG. 15. The average speed for defects and grain boundaries. From top to bottom, the curves have the form $v_0 \times t^{-x}$ with v_0 being a constant. From top to bottom, $x = 0.35 \pm 0.01$, $x = 0.41 \pm 0.01$ and $x = 0.48 \pm 0.01$. Averaged over 56 independent trials.

We also measured the average speed of the point defects and grain boundaries as a function of time after the quench, as is shown in Fig. 15. The average speed of point defects decreases as $\sim t^{-0.48}$; the average speed of grain boundaries goes as $\sim t^{-0.35}$. The scattering of the points at late stages is due to the small data sample at those times..

VI. SUMMARY

We have studied the dynamics of the defect structures in the SH model after quenches to zero temperature with a control parameter of $\epsilon = 0.1$. We find in agreement with earlier workers that the kinetics in the ordering regime, before finite-size effects enter, are dominated by the existence of moving and coalescing grain boundaries. In this regime the average size of these grain boundaries is growing and they are relatively mobile. Under the influence of finite size effects these grain boundaries shrink, the system becomes anisotropic and the ordering process speeds up.

We also measured the speed distribution of all structures that appear in the system. The average speed is decreasing as a power law and the distributions show a power-law behaviors at large speeds. However we can only get a rough estimate due to the poor statistics.

Let us return to the question of whether the SH model gives a good description of the physical system studied by Harrison, et al. [2,3]. The SH model, for small control parameter ϵ, does give coarsening with an exponent in roughly the same range as in the experiment ($1/4 \sim 1/3$). The ordering is constrained to be slower then the picture where one has a simple point defect pair annihilation process. However, the defect structures in the SH model and experiment appear quite different. The disclination quadrupole annihilations seen in experiments are not observed in the late stages of the evolution of the SH model. In the SH model grain boundaries dominate the evolution in the scaling regime, but these structures appear to play a limited role in the experiments. We must make clear that our numerical results are for systems with many fewer roll periods compared to the experimental systems (10^2 compared to 10^5), so it is possible that things change as we increase the size of the ordering system. However, our study of 256 and 512 systems shows that they differ only in the time when the finite-size effect enters. This indicates that a even larger system will display the same behavior except that the finite-size effect enters at a even later time. So we conclude that the SH model does not give a physically faithful description of the ordering in the experimental system. This raises the provocative question: Are there many different types of scenarios for ordering striped systems? We will address this question by looking at other competing models for striped formation elsewhere.

APPENDIX A: THE ALGORITHM FOR PICKING OUT DEFECTS AND FINDING DOMAIN WALLS

Hou, *et al.* [6] proposed a method, the HSG method, to measure the length of grain boundaries. They computed

the quantity $A^2 \equiv \psi^2 + (\nabla\psi)^2/q_0^2$, and if the calculated A^2 is bigger than an upper filter $0.7 \times Max(A^2) + 0.3 \times AVG(A^2)$ or smaller than a lower filter $0.7 \times Min(A^2) + 0.3 \times AVG(A^2)$, that point is counted as belonging to a domain wall. When ϵ is small, this method gives quite good results.

However, when ϵ increases, the original filters are no longer applicable. They fail to pick out most of the points and the filters must be re-chosen. For example, at $\epsilon = 0.6$, the filters $0.5 \times Max(A^2) + 0.5 \times AVG(A^2)$ and $0.5 \times Min(A^2) + 0.5 \times AVG(A^2)$ can give a satisfying result; while for $\epsilon = 0.75$, $0.4 \times Max(A^2) + 0.6 \times AVG(A^2)$ and $0.4 \times Min(A^2) + 0.6 \times AVG(A^2)$ are the better choices. Sometimes this method is unable to pick out all the defects for any choice of filter.

We introduce here a method which works for all ϵ and picks out all of the defects and nothing more.

First let us define some useful quantities. Suppose the system is discrete on the xy plane, with $\mathbf{x} = (i,j)$ (square lattice). At a fixed time, starting from the order parameter field $\psi(\mathbf{x}) = \psi_{i,j}$, we can define a director field $\hat{n}(\mathbf{x})$ as given by Eq.(11) where $\nabla\psi(\mathbf{x})$ is defined by the usual finite difference scheme, i.e.

$$\nabla\psi(\mathbf{x}) = \left(\frac{\psi_{i+1,j} - \psi_{i-1,j}}{2\,\Delta r}, \frac{\psi_{i,j+1} - \psi_{i,j-1}}{2\,\Delta r} \right) , \quad (A1)$$

where Δr is the lattice space of the system. In two-dimensional cases the nematic order parameter, $Q_{\alpha\beta}$ is completely specified by the angle

$$\varphi(\mathbf{x}) = 2\,\theta(\mathbf{x}) , \quad (A2)$$

where

$$\theta(\mathbf{x}) = \arctan\left(\frac{\hat{n}_y(\mathbf{x})}{\hat{n}_x(\mathbf{x})} \right) . \quad (A3)$$

Rather than using $\varphi(\mathbf{x})$ given by the two equations above we introduce some local smoothing. First we compute

$$\begin{aligned} \hat{B}_y &= \sin\varphi(\mathbf{x}) = 2\hat{n}_x(\mathbf{x})\hat{n}_y(\mathbf{x}) , \\ \hat{B}_x &= \cos\varphi(\mathbf{x}) = 2\hat{n}_x(\mathbf{x})^2 - 1 . \end{aligned} \quad (A4)$$

Then we smooth these two fields using the iterative process:

$$f_{(n+1)}(i,j) = \frac{1}{2}f_{(n)}(i,j) + \frac{1}{8}\sum_{(i',j')\in NN} f_{(n)}(i',j') , \quad (A5)$$

where $f_{(n)}$ is $\sin\varphi$ or $\cos\varphi$ after n iterations, and NN means the 4 nearest neighbors of (i,j) on the square lattice. This process will suppress the small fluctuations of $\varphi(\mathbf{x})$ away from the defects, while the variation of of $\varphi(\mathbf{x})$ near a defect core remains large. Our calculations show that 5 iterations provides a sufficiently smooth set

of fields for our purposes. In the next step, we calculate $\varphi(\mathbf{x})$ from $\sin\varphi(\mathbf{x})$ and $\cos\varphi(\mathbf{x})$ using

$$\varphi(\mathbf{x}) = \arctan\left[\frac{\sin\varphi(\mathbf{x})}{\cos\varphi(\mathbf{x})} \right] , \quad (A6)$$

where we adopt the convention that $-\pi < \varphi(\mathbf{x}) < \pi$.

In picking a filter we want to look at the spatial variation of the $\varphi(\mathbf{x})$ field. $\nabla\varphi(\mathbf{x})$ can be evaluated as for $\nabla\psi(\mathbf{x})$. However, there is a subtlety here. For example, if $\varphi_{i+1,j} = \pi - \delta\phi_1$ and $\varphi_{i-1,j} = -\pi + \delta\phi_2$, where $\delta\phi_1$ and $\delta\phi_2$ are small angles, then the difference between the nematic tensor $Q_{\alpha\beta}(i+1,j)$ and $Q_{\alpha\beta}(i-1,j)$ should be a small quantity. But $(\varphi_{i+1,j} - \varphi_{i-1,j})/2 = \pi - (\delta\phi_1 + \delta\phi_2)/2 \sim \pi$, which means that if we calculate the change rate of $\varphi(\mathbf{x})$ in exactly the same way as Eq.(A1), we will get a wrong answer in this context. To avoid such a problem, we define the difference between $\varphi(\mathbf{x})$ and $\varphi(\mathbf{x}')$ as the quantity with the smallest absolute value among the choices $\varphi(\mathbf{x}') - \varphi(\mathbf{x})$ and $\varphi(\mathbf{x}') - \varphi(\mathbf{x}) \pm 2\pi$. And we use this quantity in determining

$$A(\mathbf{x}) = |\nabla\varphi(\mathbf{x})|^2 \quad (A7)$$
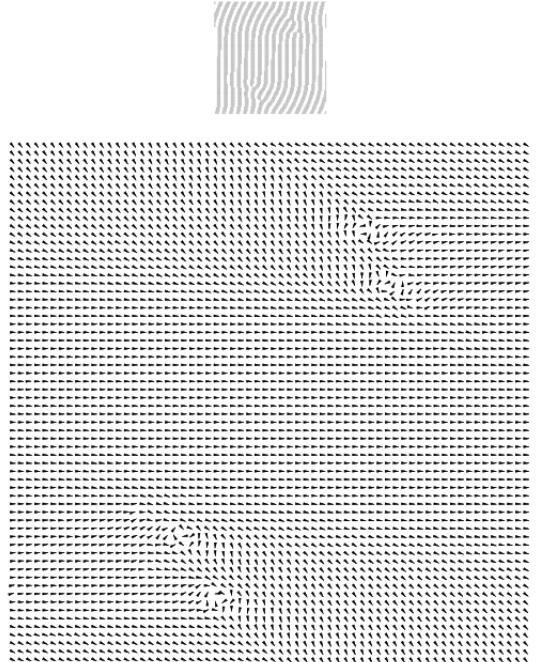
which is the key quantity in our analysis.

FIG. 16. In the lower graph, the vector field $(\cos\varphi(\vec{x}), \sin\varphi(\vec{x}))$ for the order parameter field shown above. The components of the vector field have been smoothed over 5 iterations. The lattice spacing is $\pi/4$, which means there are 8 points in one period of the layers. Not all the vectors on the lattice are shown.

Our method is based on the observation that at the core region of a defect (dislocation, disclination or part of a domain wall) the angle field $\varphi(\mathbf{x})$ changes rapidly, while in the region away from the defect's core the $\varphi(\mathbf{x})$ field is rather smooth, as can be seen in Fig. 16. Thus we can conclude with confidence that those points with larger change rates of $\varphi(\mathbf{x})$ must belong to some defect's core region or a part of a grain boundary.
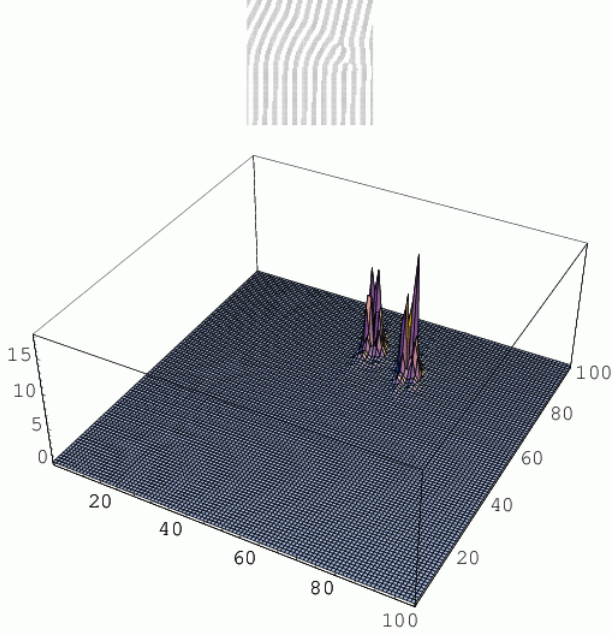

FIG. 17. In the lower graph, the scalar field $A(\vec{x})$ is plotted. This corresponds to the order parameter field shown above. $A(\vec{x})$ is sharply peaked at the core regions of the defects.

We find that $A(\mathbf{x}) \approx 0$ away from defects, but increases very rapidly in the vicinity of any defect. An example is given in Fig. 17. Therefore as long as $A(\mathbf{x})$ is large enough, we can identify the point $\mathbf{x} = (i, j)$ as part of the core region of a defect. Naturally we set up a threshold A_0, and any point with $4(\Delta r)^2 \cdot A(\mathbf{x}) > A_0$ is counted as belonging to some defect's core. Because the value of $A(\mathbf{x})$ is much larger in the defects' cores than at any other places, a range of values of A_0 can be used to find the positions of the defects core regions. With a smaller threshold the program will pick out more points in the core regions, and with a larger one it will pick out fewer points in the core regions. Our experience shows that if A_0 takes the value of $2 \sim 10$, the program picks out the same defects cores and grain boundaries. As is shown in Fig. 18 and Fig. 19, it picks out all the defects without irrelevant points.
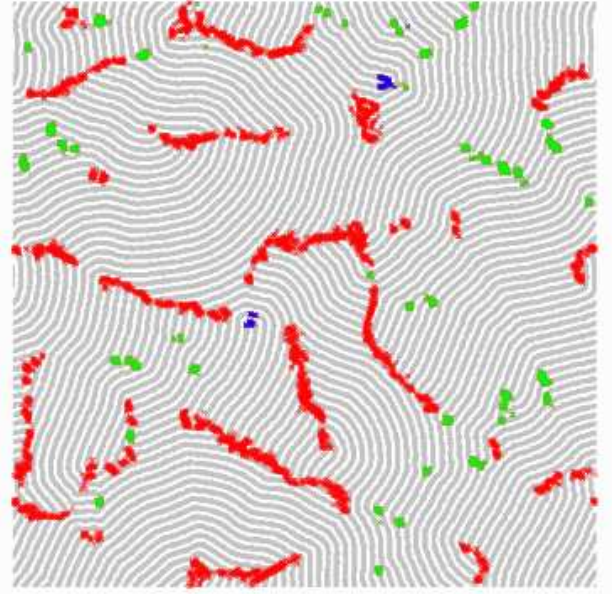

FIG. 18. Identification of all the defects in a 512×512 system ($\epsilon = 0.1$) with a threshold $A_0 = 3.5$. At each defect core region, the A field for many points exceeds the threshold. The red points belong to domain walls, the green ones belong to dislocations and the blue ones belong to disclinations.
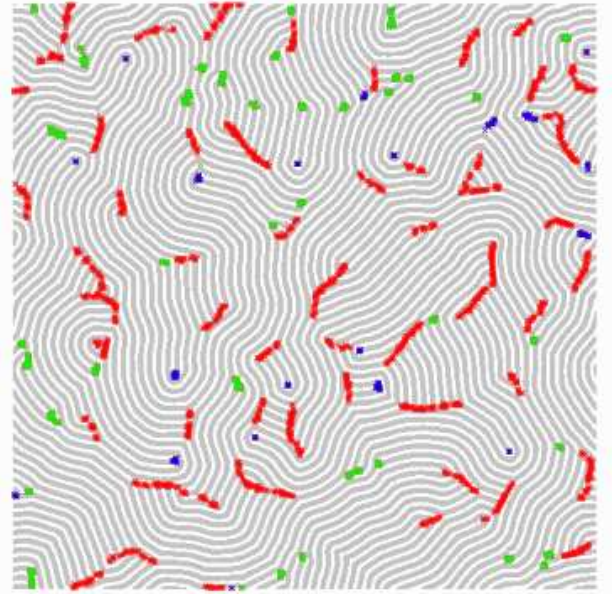

FIG. 19. Identification of all the defects in a 512×512 system ($\epsilon = 0.5$) again with a threshold $A_0 = 3.5$. Apparently the defect's density in this system is greater than the density in Fig. 18. The domain walls are much smaller for the system with larger ϵ. There are no domain walls for $\epsilon > 0.6$.

After we have used the above algorithm to pick out the points in the core regions of the point defects and grain boundaries, we can distinguish between these two structures. The difference between them is obvious. The point

defects are compact in space while the grain boundaries are ramified.

First, we must group the points we have identified according to whether or not they are in the same structure. The points in one point defect core or grain boundary are picked out because the director field changes drastically on those sites. They are very near to each other. However, they may not be neighbors. So we define a filter a_0, and when any two points' distance is less than a_0, they are supposed to be in the same defect or grain boundary's core region. We use the cluster multiple labeling method of Hoshen and Kopelman [17] to pick out such point clusters. Thus given the system's status at any time, we can find those sets of points corresponding to each individual defect or grain boundary.

Now we measure the approximate size of these structures and then distinguish between point defects and grain boundaries. We use the number of the points in the set as the size of the corresponding structure. This approximation reflects the actual size of the defect or grain boundary quite well. Then we define a filter l_0, and when the structure's size is larger than l_0, we regard the corresponding structure as a grain boundary, otherwise it's taken to be a point defect (dislocation or disclination).

We employed $a_0 = 5\,\Delta r$ where Δr is the lattice spacing and $l_0 = 18$. The results are quite satisfying.

After we have picked out the point defects, we can devide them into disclinations and dislocations. We follow Harrison's method [2,3]. Given the angle field $\varphi(\mathbf{x})$ computed in Eq.(A6) after the smoothing process, we do an integral of the variation of $\varphi(\mathbf{x})$ over a counterclockwise close path around the "mass-center" of a point defect, which is defined below. The condition for a defect to be a disclination is

$$\oint \frac{\partial \varphi}{\partial s}\, ds = \pm 2\pi \qquad (A8)$$

The integral is zero if the defect is a dislocation. To make the computation easier, we choose a 16×16 square with the mass-center at its center as the integration route.

To record the motion of one single defect or grain boundary, we track the motion of the corresponding point set's "mass center", which is defined as follows. Suppose the point set has n points with coordinates $\mathbf{r}_i, i = 1, 2, ..., n$. Then the "mass center" of the point set is defined as $\mathbf{r} = \sum_i \mathbf{r}_i/n$, just like the usual mass center definition in classical mechanics but with all masses equal to one.

In the evolution of the SH model, we sample the system every 500 time steps (in our case this is equal to 15 dimensionless time units), which is a quite short-time period in the simulation. We then identify all the dislocations, disclinations and grain boundaries, distinguish among them, and compute their *centers of mass*. Suppose at time t_1, we have the set of *mass centers*

$P = \{\mathbf{p}_i, i = 1, 2, ..., n_1\}$, and at time t_2, the "mass center" set is $Q = \{\mathbf{q}_j, j = 1, 2, ..., n_2\}$; usually $n_1 \neq n_2$. Define $d_{PQ}(i,j) = |\mathbf{p}_i - \mathbf{q}_j|$. We assume that the defects and grain boundaries do not move much in such a short time period. So if there exist two integers $k \in [1, n_1]$ and $l \in [1, n_2]$, such that

$$d_{PQ}(k,l) = \min_{j\in[1,n_2]} d_{PQ}(k,j) = \min_{i\in[1,n_1]} d_{PQ}(i,l)\,, \quad (A9)$$

it is quite reasonable to believe that $\mathbf{p}_k$ and $\mathbf{q}_l$ are just the same defect's or grain boundary's "mass center" at two successive times. Using this method, we are able to find out the trajectories of the "mass centers" as time goes on. Not all points in P and Q can be grouped into such pairs. On the one hand, this is because $n_1 \neq n_2$; on the other hand, this is also due to the criterion (A9) applied onto $\mathbf{p}_k$ and $\mathbf{q}_l$. Physically, this is consistent with the phenomena of the defect annihilation and the combination, split and shrinkage of grain boundaries.

APPENDIX B: MEASUREMENT OF THE NEMATIC CORRELATION FUNCTION

To probe the stripes' increasingly orientational order, we define the correlation function which is similar to the one employed by Christensen and Bray [10].

$$C_{nn}(\mathbf{r}, t) = \frac{1}{N^2} \sum_{\mathbf{x}} \langle \cos\left[\varphi(\mathbf{x}+\mathbf{r}, t) - \varphi(\mathbf{x}, t)\right]\rangle$$

$$= \frac{1}{N^2} \sum_{\mathbf{x}} \langle \cos\varphi(\mathbf{x}+\mathbf{r}, t) \cdot \cos\varphi(\mathbf{x}, t)\rangle +$$

$$+ \frac{1}{N^2} \sum_{\mathbf{x}} \langle \sin\varphi(\mathbf{x}+\mathbf{r}, t) \cdot \sin(\mathbf{x}, t)\rangle\,, \qquad (B1)$$

where N^2 is the area of the system and the angular brackets denote the statistical average over different initial conditions. The definition of the angle $\varphi(\mathbf{x})$ is given in appendix A.

Now in Eq.(B1) the function has been split into two parts which have the same form

$$G(\mathbf{r}, t) = \frac{1}{N^2} \sum_{\mathbf{x}} \langle f(\mathbf{x}+\mathbf{r}, t) \cdot f(\mathbf{x}, t)\rangle\,, \qquad (B2)$$

with $f(\mathbf{x}, t) = \cos\varphi(\mathbf{x}, t)$ and $f(\mathbf{x}, t) = \sin\varphi(\mathbf{x}, t)$ separately. Eq.(B2) can be easily calculated by fast Fourier transformation (FFT). First FFT $f(\mathbf{r}, t)$ to obtain its Fourier components $\tilde{f}(\mathbf{k}, t)$. Then $\tilde{G}(\mathbf{k}, t) = \langle |\tilde{f}(\mathbf{k}, t)|^2 \rangle$, and inverse Fourier transformation gives $G(\mathbf{r}, t)$. We compute the two parts in Eq.(B2) separately, and then add to obtain the correlation function $C_{nn}(\mathbf{r}, t)$.

[1] C. Bowman and A. C. Newell, Rev. Mod. Phys. **70**, 289 (1998).

[2] C. Harrison, D. H. Adamson, Z. Cheng, J. M. Sebastian, S. Sethuraman, D. A. Huse, R. A. Register and P. M. Chaikin, Science **290**, 1558 (2000).

[3] C. Harrison, Z. Cheng, S. Sethuraman, D. A. Huse, P. M. Chaikin,, D. A. Vega, J. M. Sebastian,, R. A. Register, and D. H. Adamson, Phys. Rev. E**66**, 011706 (2002).

[4] J. Swift and P. C. Hohenberg, Phys. Rev. A **15**, 319 (1977).

[5] A. J. Bray, Adv. Phys. **43**, 357 (1994).

[6] Q. Hou, S. Sasa, and N. Goldenfeld, Physica A **239**, 219 (1997).

[7] D. Boyer and J. Viñals, Phys. Rev. E **64**, 050101 (2001).

[8] Y. Pomeau and P. Manneville, J. de Phsique – Lett., **40** (23), L-609 (1979).

[9] Assume that the total area of defects and grain boundaries is $a(t)$, and $\langle \psi^2 \rangle$ in those regions is a constant χ^2, which is smaller than $\langle \psi_0^2 \rangle$. Then approximately $\langle \psi^2 \rangle_t = \frac{1}{S} \left[\langle \psi_0^2 \rangle \cdot (S - a(t)) + \chi^2 \cdot a(t) \right] = \langle \psi_0^2 \rangle - a \cdot \frac{\langle \psi_0^2 \rangle - \chi^2}{S}$, i.e. $\Delta \psi^2(t) = \langle \psi_0^2 \rangle - \langle \psi^2 \rangle_t \propto a(t)$. Since the energy should concentrate on the defects and grain boundaries, it is reasonable to expect that $a(t) \propto \Delta E(t) \propto L_E^{-1}(t)$, which is supported by the simulations. So $\Delta \psi^2(t) \propto L_E^{-1}(t)$. $L_E(t)$ and $L_\psi(t)$ are expected to have the same growth exponent. This is also supported by our simulations.

[10] J. J. Christensen and A. J. Bray, Phys. Rev. E **58**, 5364 (1998).

[11] K. R. Elder, J. Viñals, and M. Grant, Phys. Rev. Lett. **68**, 3024 (1992).

[12] J. Toner and D. R. Nelson, Phys. Rev. B **23**, 316 (1981).

[13] M. C. Cross and D. I. Meiron, Phys. Rev. Lett. **75**, 2152 (1995).

[14] D. Boyer and J. Viñals, Phys. Rev. E **63**, 061704 (2001).

[15] D. Boyer and J. Viñals, Phys. Rev. E **65**, 046119 (2002).

[16] One may doubt that the domain walls break up at this time so that their sizes decrease. However if this was true, the number of domain walls would increase, which is obviously wrong, as is shown in Fig. 10. So the main effect that decreases the size of the domain walls is the shrinkage.

[17] H. Gould and J. Tobochnik, *An Introduction to Computer Simulation Methods, Part 2*, Addison-Wesley Publishing Company (1988).